WING MOUNTED HYDROGEN FUEL TANKS: MITIGATING THE AEROELASTIC PENALTIES OF DRY WING CONFIGURATIONS?

Fintan Healy[1]**, Huaiyuan Gu**[1]**, Djamel Rezgui**[1]**, Jonathan Cooper**[1]

[1]University of Bristol
School of Civl Aerospace and Design Engineering,
Bristol, BS8 1TR, United Kingdom
fintan.healy@bristol.ac.uk

Keywords: Conceptual aircraft design, liquid hydrogen, wingbox sizing, aircraft loads, aeroelasticity

Abstract: The aviation industry's desire to mitigate its environmental impact has re-invigorated research into hydrogen-powered aircraft concepts. The transition to liquid hydrogen (LH_2) fuel results in large, cryogenic fuel tanks that cannot be accommodated within the wingbox structure, leading to fuel-free or 'dry' wings. In traditional kerosene-powered configurations fuel stored in the wings provides inertial relief, reducing the loads experienced during flight and, therefore, the required structural mass. Wing-mounted fuel tanks could be used to regain this inertial relief, and this paper investigates the aerodynamic and structural implications of integrating wing-mounted hydrogen fuel tanks into medium-sized commercial aircraft with high aspect ratio wings. A multidisciplinary conceptual aircraft sizing methodology is used to explore the effect of different fuel tank configurations - where LH_2 is stored within the fuselage, or in external wing-mounted tanks - on an aircraft's geometry and performance metrics, such as fuel efficiency. The sizing of the wingbox structure includes the numerical simulation of manoeuvre, gust and turbulence loads using an aeroelastic model. The findings suggest that while wing-mounted tanks offer inertial relief, reducing wing mass by over 20%, the increased parasitic drag from the external fuel tanks outweighs the reduction in lift-induced drag. This conclusion was observed between aspect ratios of 8 and 20, suggesting that permanently attached wing-mounted fuel tanks are not viable for hydrogen-powered aircraft with high aspect ratio wings.

1 INTRODUCTION

The current drive for sustainable aviation has renewed interest in hydrogen-powered aircraft, offering a promising avenue to reduce the aviation industry's climate impact by eliminating in-flight carbon emissions and reducing the production of nitrogen oxides (NOx) [1]. This approach holds significant potential for medium to long-range commercial flights by replacing conventional kerosene with cryogenically stored liquid hydrogen (LH_2). However, the cost per megajoule of LH_2 will likely remain higher than that of existing kerosene fuels [1]. Therefore, the fuel efficiency of future aircraft must be increased to maintain similar operating costs to those of existing designs. To this end, future aircraft designs will likely include much higher aspect ratio wings (HARW) to reduce lift-induced drag and, therefore, the total fuel burn across a typical flight.

However, increasing an aircraft's wingspan is a challenge from a structural perspective, as it requires more material to support the increased loads. This increases the aircraft's mass, requiring more lift (and, therefore, drag) to support in flight. This trade-off typically leads to an

optimal aspect ratio at which the increased mass of further increasing the wingspan outweighs the reduction in induced drag [2, 3].

In kerosene-powered aircraft, fuel is typically stored within the wing. The mass of this fuel provides inertial relief, reducing the maximum loads seen during manoeuvres and gust encounters, which mitigates the required increase in wing mass with aspect ratio. For hydrogen-powered aircraft, the lower energy density of liquid hydrogen necessitates larger fuel stores within the aircraft structure. Furthermore, minimising the surface-to-volume ratio of these fuel tanks is crucial as it reduces both the tank's weight and the heat flux between the cryogenic liquid and the outside environment. For these reasons, most studies aim to place cylindrical tanks at the front, rear or above the passenger cabin [1]- resulting in fuel-free (or 'dry') wings. This loss of inertial relief presents a challenge when sizing the aircraft's structure, meaning hydrogen-powered aircraft will likely require heavier wings with a lower optimal aspect ratio.

Another fuel-storage concept that has been suggested is the use of wing-mounted external hydrogen fuel tanks [4, 5]. Similar storage devices are regularly used to extend the range of kerosene-powered military aircraft (Fig. 1) - with these additional tanks being called 'drop-tanks'. Wing-mounted fuel tanks have also been featured on civilian aircraft, such as the Learjet 35 (Fig. 2), with such a design providing inertial relief at the cost of increased drag due to both the increased wetted area and the aerodynamic interaction between the wing and tank, with experimental results from the 1950s suggesting wingtip tanks can reduce a wings lift-to-drag ratio by 10% [6].

Previous researchers who considered using external hydrogen fuel tanks have generally concluded that the additional drag from the external tank outweighs the benefits [4, 5]. However, these results have either not considered the reduction in wing mass due to the pod [5] or have been restricted to wingspans similar to those of current-generation aircraft. However, it is envisaged that the inertial relief provided by wing-mounted fuel tanks may be more significant at greater wingspans; therefore, this paper will expand on these previous studies by exploring the effect of external fuel tanks on aircraft performance with an increased wingspan.

The sizing algorithm, presented in Section 2, considers the sizing of the entire aircraft and uses a combination of class-I and class-II sizing methodologies [7] to estimate the geometry and mass of a tube and wing configuration. The mass of most of the aircraft components is estimated using empirical relations; however, the mass of the wing structure is estimated using numerical simulations of manoeuvres and gust encounters (with the latter typically omitted in conceptual sizing studies).

The paper then sizes a medium-sized hydrogen-powered aircraft across a range of aspect ratios with wing-mounted fuel drop tanks. To determine the optimal distribution, liquid hydrogen will be distributed between an aft-fuselage tank and drop tanks in fractions between zero and 100%. Sensitivity studies are also performed for key sizing parameters, and the optimal aspect ratio of each configuration is assessed by measuring the fuel burn across a typical mission.

Figure 1: Image of an F-16C Fighting Falcon, with wing mounted drop tanks.[1]

Figure 2: Image of a Learjet 35, featuring wingtip fuel tanks.[2]

2 CONCEPTUAL AIRCRAFT SIZING METHODOLOGY

This section describes the development of a software package capable of the conceptual sizing of aircraft following the European Aviation Safety Agency's *Certification Specification for Large Aeroplanes* (CS-25) [8] and *Easy Access Rules for Air Operations* [9]. The developed package uses a combination of empirical and semi-analytical methods to size "tube-and-wing" style aircraft powered by the combustion of either hydrogen (LH_2) or kerosene (JA1[3]),

The paper utilises the A320neo as a reference aircraft, with its top-level aircraft requirements (TLARs) presented in Table 1. Therefore, the described sizing algorithm is tailored for A320-like aircraft operating on similar missions with a comparable technology level(e.g. the primary structure is made of aluminium alloy).

The algorithm was primarily developed to investigate the effect of three key design variables: the type of fuel, wing aspect ratio and fuel store location, which are depicted in Fig. 3. Concerning LH_2 powered aircraft, the percentage of liquid hydrogen stored in wing-mounted drop-tanks is denoted as η_p, with a value of zero indicating no drop-tanks and one indicating no aft fuel tank. The spanwise location of the drop tanks is also explored, and the normalised position of the tank, with respect to the inner wingspan (b_h), is defined as η_b.

In configurations in which the wingspan is greater than $36\,\mathrm{m}$, ground folding wingtips will be included to ensure the aircraft has the same ICAO Aerodrome reference code as the A320, and it is assumed the drop-tanks are always mounted inboard of a ground folding wingtip.

2.1 Algorithm Overview

The sizing of aircraft is an inherently multi-disciplinary process, and an overview of the algorithm used in this paper is shown in Fig. 4 in the form of an extended design structure matrix (XDSM) [10]. The green blocks on the diagonal represent the analysis of different disciplines, with the numbering of these blocks indicating their execution order. Variables emanating laterally from each discipline represent the outputs which other analysis modules depend on[4] and the

---

[1]Copyright Chris Lofting `https://www.airliners.net/photo/Greece-Air-Force/Lockheed-Martin-F-16CJ-Fighting-Falcon/1309901` [accessed 26/05/2024]

[2]Copyright Bjoern Huke `https://www.jetphotos.com/photo/10932445` [accessed 26/05/2024]

[3]JA1 is an abbreviation of Jet A-1 fuel.

[4]For example, the mission analysis module relies on the operational empty mass (OEM) calculated in the Geometry Builder and outputs the required fuel mass (M_f) and landing mass (M_{ld})
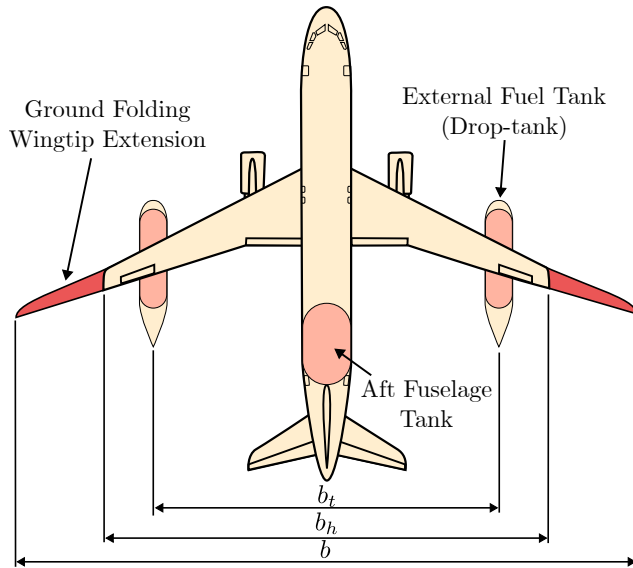
Figure 3: Representation of the key configuration variables explored during this paper.

Table 1: Top Level Aircraft Requirements For an A320-like Aircraft

Parameter	Value	Unit
PAX (single class)	180	-
Maximum Payload	19.3	t
Harmonic Range	2450	nm
Cruise Altitude	34000	ft
Cruise Mach	0.78	-
Maximum Wingspan	36	m
V_{climb} [CAS]	150	m/s
V_{app} [CAS]	129	m/s
$(T/W)_{TO}$	0.31	-
M_{Lnd}/S	550.7	kg/m^2

orange rounded blocks represent convergence loops. The algorithm presented in Fig. 4 uses two convergence loops, each ensuring consistency of the estimated maximum take-off mass. The inner convergence loop iterates over computationally 'cheap' disciplines, whereas the outer loop runs computationally 'expensive' disciplines.

The following subsections outline the methodology and assumptions used in each of the analysis modules. It is worth emphasising that the methodology used in each of these modules is not novel and is instead based on the content of multiple books [5, 7, 11, 12] and research articles [2, 13–16]. Furthermore, similar - and in many cases more mature - aircraft sizing tools have already been presented in the literature. Some of these tools are not available to the wider research community (such as openAD from DLR [17] and the Aircraft Design Initiator from Delft University [9]), some are available on request (such as NeoCASS from Poitecnico di Milano [18]) and others are open-source, such as SAUVE from Stanford University [15], or Aviary from NASA.[5]

The rationale for not using these existing tools was driven by the ease of integration of the wingbox sizing tool described in Section 2.7, which uses MSC Nastran simulations to estimate manoeuvre, gust and turbulence loads.

With all this in mind, the following sub-sections are not intended to provide new insights to the reader; however, by describing the analysis in detail, we aim to offer a transparent understanding of the chosen approach's strengths and weaknesses, allowing readers to replicate and draw their own conclusions about the results presented in this paper.

2.2 Entry Point

The top-level entry requirements (TLARs) shown in Table 1 and the general masses of the reference aircraft (Table 2) were used as an initial starting point for the sizing algorithm.

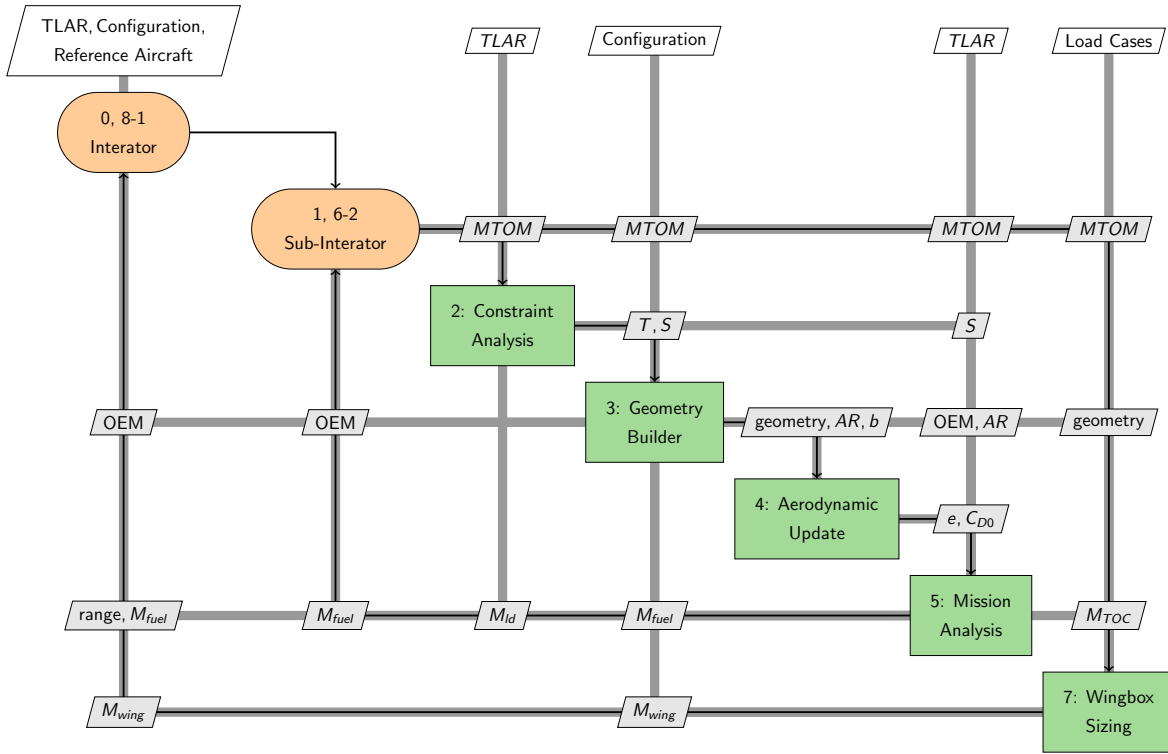[5]https://github.com/OpenMDAO/Aviary [accessed 24/05/2024]

Figure 4: Extended design structure matrix (XDSM) showing the workflow of the sizing algothrim.

Table 2: Reference aircraft typical values [19].

Parameter	Value	Unit
Maximum Take-off Mass	79.0	t
Maximum Landing Mass	67.4	t
Operational Empty Mass	45.0	t
Maximum Fuel Mass	18.7	t
Thrust-to-Weight Ratio	0.31	-

2.3 Constraint Analysis

Typically, constraint analysis in conceptual aircraft sizing uses a series of equations that predict cruise, climb, take-off and landing performance to estimate the required thrust-to-weight ratio and wing loading for a given configuration [11]. A simplified version of this process is utilised here, in which the required wing loading and thrust-to-weight ratio remain constant, with values derived from the reference aircraft (Table 2). Hence, given an assumed maximum landing mass (M_{LD}) and wingspan (b), the required static thrust (T), wing area (S) and aspect ratio (AR) can be calculated. These assumptions were chosen to minimise the dimensionality of the sizing process, enabling the dependency between other parameters to become clearer.

2.4 Geometry and Mass Estimation

The aircraft geometry estimation is split into subroutines for the fuselage, wing, empennage, propulsion and landing gear. The following subsections outline the process used in each of these disciplines. Additionally, section 2.4.1 outlines the process used to estimate the mass of a liquid hydrogen fuel tank.

2.4.1 Liquid Hydrogen Fuel Tank Mass Estimation

As the boiling point of hydrogen is around $20\,\mathrm{K}$, liquid hydrogen storage requires fuel tanks with low surface area to volume ratios and significant thermal insulation between the fuel and the external environment. As liquid hydrogen absorbs energy from the environment, it evaporates, rising into a gaseous upper region of the fuel tank, known as the *ullage*. As more hydrogen evaporates, the pressure of the ullage increases; if this pressure reaches the structural limit of the tank (known as the venting pressure, p_v), the ullage must be vented. The minimum pressure of the ullage must also be kept above atmospheric pressure; this prevents the ingress of air (and moisture) into the fuel tank, which could result in fuel combustion.

Venting pressure and insulation thickness are selected as trade-offs between tank mass, insulation mass, and hydrogen lost through venting throughout a mission. For this paper, a constant venting pressure of $250\,\mathrm{KPa}$ and an insulation thickness of $12\,\mathrm{cm}$ will be assumed, which are in line with those of previous studies [4, 14, 20].

The tank mass estimation outlined below closely follows that of [14]. The shape of $\mathrm{LH_2}$ fuel tanks will be assumed to be cylindrical with ellipsoidal end caps with a 2:1 major to minor axis ratio. For a given total length (L), radius (r) and venting pressure, the wall thickness (t_s) can be estimated using Barlow's formula, such that

$$t = \mathrm{SF}\,\frac{(p_v - p_{out})r}{\sigma} \tag{1}$$

where p_{out} is the external air pressure, SF is the applied safety factor and σ is the wall's allowable stress. For this paper, values obtained by [5] are utilised, in which the maximum allowable stress of an aluminium alloy is assumed to be $172.4\,\mathrm{MPa}$, which represents a fatigue quality index of 5, a 50,000-hour service life, and a life reduction factor of 4.

Given the thickness of the insulation and the tank wall, the total usable fuel volume can be calculated minus the following provisions [5, 14, 20]:

- A 3% ullage at maximum load to allow for controllable increases in ullage pressure due to unforeseen expansion or heating of the fuel.

- A 0.6% internal equipment allowance
- A 0.9% tank contraction allowance
- A 4.6 % unusable fuel allowance, which includes a 0.3 % allowance for the volume of fuel in the fuel system and a 4.3% pressurisation fuel allowance, which is an approximation for the amount of gaseous hydrogen required to maintain the minimum pressure in the fuel tank at the end of the longest mission [14].

The mass of the tank can be estimated by calculating the volume of the aluminium wall and insulation and multiplying them by their respective densities ($2840 \, \mathrm{kg/m^3}$ and $32 \, \mathrm{kg/m^3}$ [14]). The unusable fuel allowance is included in the tank's mass for sizing.

For a given tank length and diameter, the process outlined in this section fully defines the internal volume and, therefore, the fuel capacity of the tank. However, during aircraft sizing, the problem is inverted, with the required fuel mass being known but not the tank's dimensions; therefore, an iterative process was used to calculate the tank geometry in each instance.

2.4.2 Fuselage

The diameter of the aircraft is assumed to be equal to that of the reference aircraft ($D_{\mathrm{cab}} = 2.02$m), and it is assumed that there are six seats per row so that the number of rows is equal to

$$N_r = \lceil \mathrm{PAX} \, / 6 \rceil \tag{2}$$

The length of the cabin is then approximated as

$$l_{\mathrm{cab}} = N_r k_{\mathrm{cab}} = 0.7632 N_r \tag{3}$$

where k_{cab} has been approximated from the single class variants of the A320 family [19, 21, 22]. The length of the cockpit, l_{cp} is assumed to be $4 \, \mathrm{m}$ and the length of the tail section (l_{tail}) is assumed to equal 1.5 times the cabin diameter. If an aft hydrogen fuel tank is required, its outer radius is assumed equal to that cabin,[6] and its length (l_{tank}) is calculated according to the required fuel mass ($M_f(1 - \eta_p)$) and the process detailed in Section 2.4.1. Therefore, the total length of the fuselage is equal to

$$l_{\mathrm{fus}} = l_{cp} + l_{\mathrm{cab}} + l_{\mathrm{tail}} + l_{\mathrm{tank}} \tag{4}$$

and the mass of the fuselage, furniture, systems and operational items are estimated using equations 8.3, 8.10, 8.9 and 8.1 in [23], respectively, such that

$$m_{fus} = 6.12 D_{\mathrm{cab}}^2 (l_{\mathrm{fus}} + 1.5) + 31.6 D_{\mathrm{cab}} L + 0.14(m_{t,fus} + m_{t,fus}) \tag{5}$$

$$m_{furn} = 1.22(l_{\mathrm{fus}} - l_{\mathrm{tank}}) D_{\mathrm{cab}} (3 D_{\mathrm{cab}} + 1.5) + 356.8 \tag{6}$$

$$m_{sys} = (27.5 D_{\mathrm{cab}} + 15.3)(l_{\mathrm{fus}} - l_{\mathrm{tank}}) \tag{7}$$

$$m_{op} = 35.68 \, \mathrm{PAX} \tag{8}$$

where all values are in base S.I. units and ($m_{t,fus} + m_{t,fus}$) is the combined mass of the fuselage fuel and aft fuel tank. Note, the characteristic length in Eqs. (6) and (7) has been modified not to include the length of the aft fuel tank and the final term in Eq. (5) has been added to improve correlations with previous studies, as discussed in section Section 2.4.1.

---

[6] an integral tank design[5]

Table 3: Hinge mass fraction as a function of normalised hinge position. Extracted from [24].

Normalised Spanwise Hinge Position	0.32	0.48	0.64	0.90	1.00
Hinge Mass Fraction ($\tilde{m}_{fold}$)	0.116	0.087	0.032	0.010	0.000

2.4.3 Wings

The quarter chord sweep angle (Λ_{qtr}) is calculated as a function of the cruise mach number (M_c), such that [7]

$$\Lambda_{qtr} = \arccos\left(\frac{3M^*}{4M_c}\right) \tag{9}$$

where M^* is the critical Mach number and represents the technology level of the wing design - for this paper, it is set to 0.935. As per the reference aircraft, it is assumed that the trailing edge sweep angle is zero degrees up to a spanwise position of $3.25\,\mathrm{m}$ (enabling the integration of landing gear and high lift devices) and the taper ratio outboard of this section is equal to 0.35.

The thickness-to-chord ratio at the root (t_c) is assumed to be equal to [7]

$$t_c = \cos\Lambda_{qtr}(M^* - 0.1(1.1C_{l,TOC}/\cos^2(\Lambda_{qtr}))^{1.5} - M_c\cos\Lambda_{qtr}) \tag{10}$$

where $C_{l,TOC}$ is the lift coefficient at the 'top of climb' on the design mission. The tip thickness-to-chord ratio is assumed to be 3 % lower than that of the root [23].

Overall, Eqs. (9) and (10) and the assumptions mentioned above fully define the planform and general thickness of the wing. The definition of the wing's primary mass and stiffness is detailed in Section 2.7, and the wing's secondary mass is estimated as 73.7% of the primary mass [16], which is assumed to be evenly distributed through the wing volume.

If the wingspan of the aircraft is greater than $36\,\mathrm{m}$, a ground folding wingtip is included such that the ground wingspan of the aircraft (with the wingtips folded up) was $35\,\mathrm{m}$. The mass of the hinge mechanism was estimated using the process outlined by [24], which captures the increased mass requirements of larger, heavier wingtips. More specifically, Table 3 contains a tabulated version of Fig. 6 in [24]; it describes the variation in the hinge mass fraction (the hinge mass as a percentage of the total wing mass) as a function of its normalised spanwise location, and an Akima spline was used to interpolate between the different values.

If a drop-tank is required, its total mass is calculated according to the required fuel mass ($M_f\eta_p$) and the process outlined in Section 2.4.1. The tank is assumed to have a slenderness ratio (length divided by max diameter) of four. The pylon mass is estimated by multiplying the total tank mass (structural + fuel mass) by 0.014. This factor has been used in a previous study [4] and is based on data from the drop-tanks used on the Lockheed C-130 Hercules.

2.4.4 Propulsion

The CFM-LEAP-1A turbofan engine was used as the reference engine for this study. Its dimensions, static thrust and mass are shown in Table 4. Due to a lack of available data, the thrust-specific-fuel-consumption (TSFC) of the reference engine is estimated during max thrust and cruise using

$$TSFC_{T,\max} = 19e^{(-0.12\,\mathrm{BPR})} \qquad \{mg/Ns\} \tag{11}$$

$$TSFC_{\mathrm{cruise}} = 25e^{(-0.05\,\mathrm{BPR})} \qquad \{mg/Ns\} \tag{12}$$

Table 4: CFM-LEAP-1A engine performance characteristics [25].

Parameter	Value	Unit
Thrust (Static)	121	kN
Mass	3008	kg
Length	3.328	m
Diameter	2.4	m
BPR	11	-

which are taken from [12]. By assuming $TSFC_{\text{cruise}}$ occurs at the design Mach number and altitude in the TLARs, the scaling approach proposed by [11] was used to estimate the TSFC at other parts of the flight envelope, such that

$$\text{TSFC}(M, \text{alt}) = (TSFC_{T,\text{max}} + BM)\sqrt{T_{\text{alt}}/T_0} \tag{13}$$

where T_0 is the standard atmospheric temperature at sea-level, T_{alt} is the atmospheric temperature at the chosen altitude, and B is a constant calculated using Eq. (12).

For a given required thrust, The dimensions and mass of the reference aircraft are scaled using the following equations

$$L = L_{\text{actual}}(T/T_{\text{actual}})^{0.4} \tag{14}$$

$$D = D_{\text{actual}}(T/T_{\text{actual}})^{0.5} \tag{15}$$

$$M = M_{\text{actual}}(T/T_{\text{actual}})^{1.1} \tag{16}$$

which are taken from [12] and where T, L, D and M stand for the thrust, length, diameter and mass, respectively. It is assumed that the TSFC is constant across any scaling process.

Regarding hydrogen-powered aircraft, in previous research, it has been considered a conservative estimate to assume the energy-specific fuel consumption is constant between kerosene and hydrogen-powered engines [4, 5, 14]. Therefore, the TSFC is scaled by the ratio of specific energies of kerosene and hydrogen ($43.2/120 = 0.36$). Furthermore, it is assumed that the mass of a hydrogen-powered engine is the same as the equivalent kerosene-powered engine.

2.4.5 Landing Gear

The mass of the landing gear was estimated using equations 15.50 and 15.51 in [12], multiplied by a scaling factor $k_{\text{gear}} = 0.85$, which has been included to improve correlations with previous studies, as discussed in section Section 2.4.1. The landing gear length was calculated to ensure enough vertical clearance between the landing gear and the engine, as per CS-25[8].

2.4.6 Empennage Planform and Wing Placement

The placement of the main wing and the sizing of the empennage are tightly linked. Therefore, their analysis is conducted in an iterative loop, as shown in Fig. 5.

The planform of the empennage is sized using fixed tail volume coefficients [12], which are derived from the geometry of the reference aircraft and the values are shown in Table 5. The area of the horizontal and vertical tail surfaces (S_{ht} and S_{vt}) are calculated as

$$S_{ht} = \bar{V}_{ht}\frac{S \cdot \text{MGC}}{x_{ht} - x_{aft}} \tag{17}$$

$$S_{vt} = \bar{V}_{vt}\frac{S \cdot b}{x_{vt} - x_{aft}} \tag{18}$$
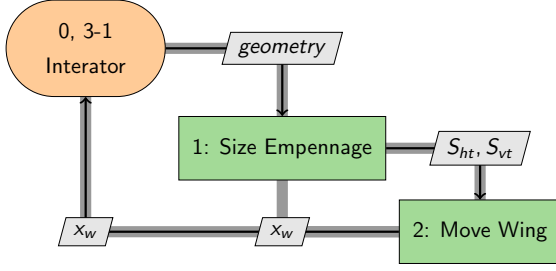
Figure 5: Empennage sizing XDSM.

Table 5: Assumed parameters for empennage sizing.

Parameter	Value
$\bar{V}_{ht}$	0.9936
$\bar{V}_{vt}$	0.0706
x_{ht} [m]	$l_{fus} - 0.75 c_{ht} - 2$
x_{vt} [m]	$l_{fus} - 0.75 c_{vt} - 2$
AR_{ht}	4.9
AR_{vt}	3.1

where MGC is the mean geometric chord of the main wing,[7] x_{aft} is the aft-most possible position of the aircraft's centre of mass, and x_{ht} and x_{vt} represent the longitudinal position of the aerodynamic centres for the horizontal and vertical tail surfaces, respectively. x_{ht} and x_{vt} are approximated from that of the reference aircraft, and the values are shown in Table 5.

The position of the main wing is chosen so that the aft-most achievable position of the aircraft's centre of mass - considering all combinations of fuel and payload - is equal to

$$x_{aft} = x_{mgc} + 0.1 \cdot \text{MGC} \tag{19}$$

e.g. the aft-most centre of mass lies 10% of the mean geometric chord behind the aerodynamic centre of the main wing.

2.5 Aerodynamic Parameter Estimation

The aerodynamic analysis module in Fig. 4 estimates the drag polar of an aircraft based on its geometry. By assuming a quadratic drag polar of the form

$$C_D = C_{D,0} + \frac{C_L^2}{\pi e_0 \, \text{AR}} \tag{20}$$

where $C_{D,0}$ is the zero-lift drag coefficient, C_L is the current lift coefficient, and e_0 is the Oswald efficiency factor, which is estimated using the procedure outlined by [26].

The zero-lift drag coefficient is estimated using the 'component build-up method' and a flat-plate analogy [12], in which $C_{D,0}$ is calculated as the summation of component level zero-lift drag coefficients, such that

$$C_{D,0} = \sum \left(C_{fe} \cdot \text{FF} \cdot Q \cdot S_{wet}/S_{ref} \right) + C_{D,p} \tag{21}$$

where C_{fe} is the skin-friction drag coefficient for each component, FF is the component form factor, Q is an interference factor and S_{wet} is the component wetted area. $C_{D,p}$ is the drag due to protuberances, and it is assumed to be equal to 2% of the total drag [12].

The skin-friction drag coefficient is dependent on the percentage of laminar flow on each component (p_{lam}). For this paper, it is assumed that laminar flow occurs over 25% of the wing and

---

[7]As explained well by [11], the mean geometric chord (MGC) is commonly referred to as the mean aero-dynamic chord (MAC). However, the term definition is based solely on geometry and has no direct relation to aerodynamic forces. For example, the spanwise position of the MGC rarely aligns with the spanwise centre of lift. Hence, in this paper, the term MGC is preferred.

Table 6: Parameters used to estimate the zero-lift drag coefficient for each component. Most values have been estimated using design rules from [12].

Component	p_{lam} [%]	FF^b	Q
Wing	25	Eq. (12.30) [12]	1
Fuselage	$10/37.6 \cdot l_{fus}$	Eq. (12.31) [12]	1
External Store	25	Eq. (12.32) [12]	1.3
Engine	25	Eq. (12.32) [12]	1.3
Empennage	25	Eq. (12.30) [12]	1.04
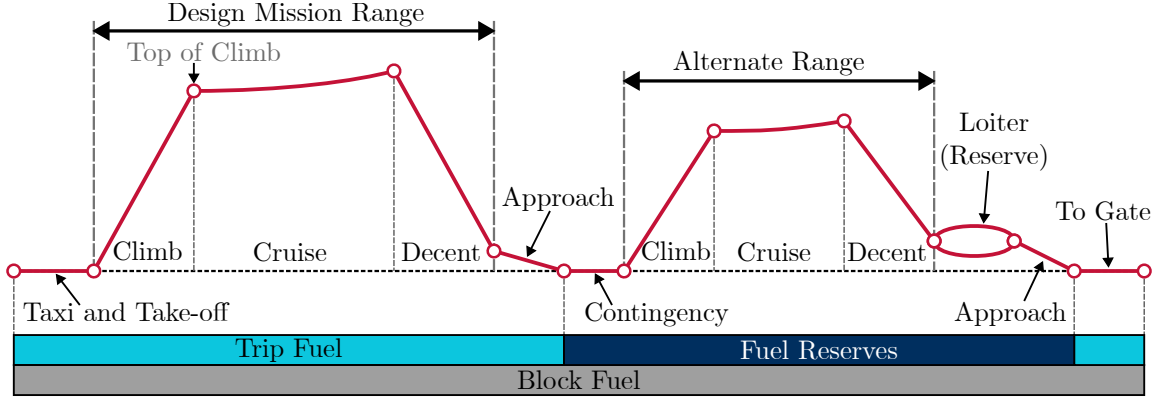
Figure 6: Design mission segment and fuel breakdown

external fuel tanks and the first $9.5\,\mathrm{m}$ of the fuselage (25% of the reference aircraft length), ensuring increases in fuselage length due to a rear fuel tank did not unfairly increase the total area of laminar flow. Other values of p_{lam} used, as well as estimates of the form factor (FF) and the interference factor (Q), can be found in Table 6.

2.6 Mission Analysis

The mission analysis module estimates the fuel required to complete a design mission. The chosen design mission is shown in Fig. 6, which adheres to the EASA Rule for Air Operations [9]. The design mission range, cruise altitude, cruise Mach number and alternate range are all specified in the aircraft TLARs. Contingency fuel is calculated as 3%

The required fuel is estimated using the process outlined by [11], where the aircraft's weight fraction is calculated across each segment of the mission. For example, the mission shown in Fig. 6 consists of 12 segments and 13 nodes. The weight of the aircraft at the i'th node is equal to

$$W_i = W_{i-1} \left(\frac{W_{i-1}}{W_i} \right) \tag{22}$$

hence, the weight of the aircraft at the final node is equal to

$$W_N = W_0 \prod_{i=1}^{N} \left(\frac{W_{i-1}}{W_i} \right) \tag{23}$$

The weight fraction during each segment of the design mission was calculated using the equations outlined in Table 7. It should be noted that

- The TSFC for each segment was calculated using Eq. (13) at the segment's mean altitude and Mach number.

11

Table 7: Mission Segment Equations

Segment	Weight Fraction	Notes
Taxi and Take-off	Equation (6-32) [11]	20 minutes taxi time, 1 minute take off time.
Climb	Equation (6-34) [11]	Split into $500\,\text{ft}$ sections
Cruise	Equation (6-35) [11]	Assume constant C_L
Decent	Equation (6-34) [11]	Assume idle power (2% thrust-to-weight ratio)
Loiter	Equation (6-36) [11]	-
Contingency	Equation (6-36) [11]	max(3% of trip fuel, 5-minute loiter)

- Climb and decent segments were sub-divided into smaller segments with a maximum altitude change of $500\,\text{ft}$. In each sub-segment, the maximum equivalent airspeed was the smaller of V_{climb} or that at the cruise Mach number (limiting the velocity at segments at lower altitudes).
- The climb rate was assumed to be $1500\,\text{ft/min}$ and the decent rate was assumed to be $2000\,\text{ft/min}$.
- If the distance travelled during climb and descent is greater than the required range, the cruise altitude is reduced in $1000\,\text{ft}$ increments until the length of the cruise component is greater than zero.

Once the mission analysis is complete, the weight fraction at the 'top of climb', landing, and all other flight points can be calculated. In particular, the trip fuel, $M_{f,trip}$, and the block fuel, $M_{f,block}$, can be estimated. The definition of both terms is shown graphically in Fig. 6; the trip fuel is the amount of fuel burned to reach the destination without a diversion, whereas the block fuel is the total fuel required, including reserves.

The specific energy consumption (SEC) of a mission is an important quantity that will be used regularly in this paper to compare configurations. The SEC represents the energy consumed per passenger per kilometre of travel; it is defined as

$$\text{SEC} = \frac{M_{f,trip} \cdot e}{\text{PAX} \cdot r_{harm}} \tag{24}$$

where e is the specific energy of the fuel and r_{harm} is the range of the harmonic mission.

2.7 Wingbox Sizing

The wingbox sizing analysis discipline uses an adaptation of the procedure outlined by [2] to size the primary wing structure. An overview of this algorithm is shown in Fig. 7; it uses an aeroelastic model to calculate the forces and moments acting along the wing during manoeuvres, gusts and turbulence encounters. The maximum loads are then used to size the primary elements of the wingbox structure and a discrete number of stations along the wingspan. A condensation process is then used to estimate the bending and torsional rigidity of an equivalent beam model, which is used to update the underlying aeroelastic model. The following subsections go into more detail about each stage of the analysis shown in Fig. 7.

2.7.1 Aeroelastic Model Generation

The aeroelastic model was generated using MSC Nastran [27]. The structural model is based on a 'stick' and lumped mass representation of an aircraft [28], with the wing discretised into a series of one-dimensional beam elements. In the first iteration of the model, these beam
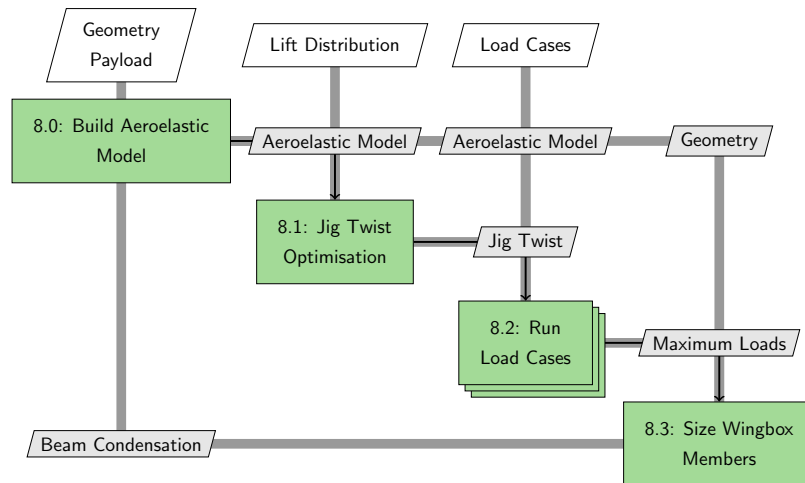
Figure 7: Extended design structure matrix (XDSM) showing the workflow of the wingbox sizing algorithm.

elements are assumed to be rigid; however, in later iterations, the sectional bending and torsional rigidity are set to those estimated from the wingbox structure.

The aerodynamic forces acting on the reference wing were modelled using an implementation of the doublet lattice method (DLM) [29–31]. This method is based upon unsteady potential flow theory and reduces to the vortex lattice method (VLM) in the steady case. The DLM assumes the flow is attached, compressible, inviscid and irrotational. Although such a method neglects nonlinear aerodynamic effects such as flow separation, shocks and boundary layers, the efficient integration of unsteady aerodynamics terms allows for the efficient evaluation of multiple flight conditions and load cases.

2.7.2 Jig Twist Optimisation

The initial aeroelastic model has zero jig-twist, leading to a non-optimal lift distribution during cruise, which increases fuel burn and affects the loads experienced by the wing structure. To remedy this, a series of static aeroelastic analyses are conducted in the steady level flight condition at the top of climb (TOC). After each analysis, the jig-twist required to achieve 1) an elliptical lift distribution and 2) an angle of incidence of 3 degrees is estimated. The process is then repeated until convergence is achieved.

2.7.3 Load Cases

The load cases considered to asses the worst-case loads expected during flight are shown in Table 8. They include a ground loading case, which simulates the aircraft on the airport apron; a series of manoeuvres at the cruise altitude; and gust and turbulence encounters at the 'crossover' altitude (which is defined as the altitude at which the Mach number and max climb calibrated airspeed, correspond to the same true airspeed). This altitude is chosen as it is where the aircraft experiences the highest dynamic pressure.

Manoeuvre loads were computed by conducting static aeroelastic analysis using the Nastran solution sequence SOL144. Peak gust loads were computed using the Nastran solution sequence SOL146, where the aircraft was subjected to a family of discrete gusts in the form of a "1-cosine" vertical gust. The selected gust profile was chosen to be the same as that in the EASA

Table 8: Load cases considered during sizing.

Load Case	Load Factor	Mode	Mach No.	Altitude	Fuel Filling Level [%]	Name
1	0	Ground Loading	0	0	100%	Gnd
2	2.5	Manuourve	M_c	Alt_c	Top of climb	M2.5
3	-1	Manuourve	M_c	Alt_c	Top of climb	M-1
4	2.5	Manuourve	M_c	Alt_c	0	M2.5_ZF
5	1	Gusts	M_c	Crossover	Top of climb	Gust
6	1	Turbulence	M_c	Crossover	Top of climb	Turb

regulations regarding civilian aircraft [8], in which the gust profile is defined as

$$\mathrm{w}_g(t) = \frac{\mathrm{w}_{\mathrm{g0}}}{2} \left(1 - \cos \frac{2\pi V t}{L_g} \right) \tag{25}$$

where L_g is the gust length, V is the true flight speed and w_{g0} is peak gust velocity, which is defined as

$$\mathrm{w}_{g0} = \mathrm{w}_{\mathrm{ref}} \left(\frac{L_g}{214} \right)^{\frac{1}{6}} \tag{26}$$

where $\mathrm{w}_{\mathrm{ref}}$ varies piecewise linearly from $17.07\,\mathrm{ms}^{-1}$ at sea level, $13.4\,\mathrm{ms}^{-1}$ at $15\,000\,\mathrm{ft}$, and $7.9\,\mathrm{ms}^{-1}$ at $50\,000\,\mathrm{ft}$. Gust lengths were varied between $18\,\mathrm{m}$ and $214\,\mathrm{m}$ in 16 linearly spaced increments. The loads given by the SOL146 solution sequence are incremental loads; therefore, the static aeroelastic loads in steady-level flight must be added to the results.

Peak turbulence loads were computed using the Nastran solution sequence SOL146. This analysis is conducted in the frequency domain and assumes that the power spectral density of the turbulence follows a Von Kármán velocity spectra [8], with a turbulence scale factor of $2500\,\mathrm{ft}$. The root-mean-squared (RMS) turbulence intensity is assumed to be $24.08\,\mathrm{m/s}$ as per [8].

2.7.4 Sizing of Wingbox Members

It is assumed that the front and rear spars are located at 15% and 65% of the chord, respectively. For simplicity, the wingbox is modelled as a rectangle, with a height equal to the mean airfoil thickness between the front and rear spars (assuming the airfoil section is a stretched version of the super-critical aerofoil SC(2)-0614).

Given the maximum bending and shear loads at each beam spanwise station, the spar caps, spar webs, skin, stringers and ribs are sized as detailed in [2]. The process consists of a series of handbook methods which ensure the structure (which is assumed to be constructed of aluminium with a Young's modulus of $97\,\mathrm{GPa}$, shear modulus of $37.3\,\mathrm{GPa}$, density of $2710\,\mathrm{kg/m}^3$ and a yield stress of $0.5\,\mathrm{GPa}$) can withstand the required loads without buckling. Additionally, a minimum thickness of $1\,\mathrm{mm}$ was set for the spar webs and caps and ribs, and $0.5\,\mathrm{mm}$ for the skin and stringers, ensuring the structure did not taper to zero thickness.

Finally, the 2D wingbox geometry at each station was condensed down to a series of one-dimensional beam properties as per Appendix A of [2].

3 VALIDATION OF ANALYSIS METHODS

The sizing methodology outlined in Section 2 is first used to size a kerosene-powered aircraft with the same TLARs as the A320neo. The resulting aircraft will then be compared to those presented in other publications which size similar aircraft.

Table 9: Top-level aircraft requirements and selected masses for the A320neo family.

Aircraft		A319 WV055	A320 WV055	A321 WV053
PAX (single class)	[-]	156	180	235
Max. Payload	[t]	17.75	19.3	25
Harmonic Range	[nm]	2720	2450	2500
$(T_W)_{TO}$	[-]	0.32	0.31	0.31
M_{Lnd}/S	[kg/m^2]	522.1	550.7	631.5
MTOM	[t]	75.5	79	93.5
OEM	[t]	42.6	45.0	50.6
Wing Area	[m^2]	122.4	122.4	122.4

Table 10: Comparison table of the A320neo family and the sized aircraft

Parameter	A321	B321-JA1	$\Delta[\%]$	A320	B320-JA1	$\Delta[\%]$	A319	B319-JA1	$\Delta[\%]$
M_{TO} [t]	93.5	93.1	0	79.0	79.0	0	75.5	75.7	0
M_{OEM} [t]	50.6	50.6	0	45.0	45.0	0	42.6	42.8	+1
M_{Lnd} [t]	77.3	78.0	+1	67.4	66.4	-2	63.9	62.5	-2
$M_{f,cap}$ [t]	18.4	18.7	+2	18.7	18.7	0	18.7	18.7	0
$M_{f,block}$ [t]	17.9	17.5	-2	14.7	14.7	0	15.2	15.2	0
$M_{f,trip}$ [t]	15.5	15.2	-2	12.7	12.7	0	13.1	13.3	+1
S [m^2]	122.4	122.4	0	122.4	122.4	0	122.4	122.4	0
l_{fus} [m]	44.5	44.5	0	37.6	36.9	-2	33.8	33.9	0
R_{ferry}[km]	6945	6747	-3	7954	7637	-4	8186	8039	-2

Even at the conceptual level, sizing an aircraft that matches a reference aircraft's size and performance is a non-trivial process. For example, aircraft are typically designed with evolvability in mind, with a margin built into the sizing of wing area, undercarriage, empennages and engines to allow for future fuselage extensions [32]. Such trends are evident in the A320neo family (which includes the A319neo, A320neo and A321neo). As shown in Table 9, although the maximum number of passengers and maximum take-off mass can vary by up to 80 passengers and 18 tonnes, respectively, the wing area, empennage size, and engine model are constant between all three aircraft.[8,9]

Therefore, the load cases of the A321 must be considered in the sizing of an aircraft equivalent to the A320. To achieve this, the TLARs of the A321, shown in Table 9, are used to initiate the sizing algorithm. Once the analysis has converged on a design, the properties of the wing, empennage, and engines are held constant, and then the sizing algorithm is restarted with the TLARs of the A320 and A319, respectively.

A comparison between the A320 family and the conceptual aircraft sized in this manner (the B3xx-JA1, where JA1 stands for Jet A-1 fuel) is shown in Table 10. Note that the wing area was fixed to that of the A321neo, and the fuel capacity of the wings and central fuselage tank was tuned to match the quoted capacities for the A320 (6.5 t in the central tank and 6.1 t in each wing). The accuracy between the reference and sized aircraft (Table 10) is well within those expected at the conceptual design stage. The main discrepancy occurs in off-design conditions such as the ferry range (max range with zero payload). However, this is likely due to a fixed cruise altitude, meaning the lighter aircraft operates at different C_l values.

---

[8]It should be noted that the increased wing loading of the A321 is somewhat compensated by the use of a more complex high-lift system (i.e. a double slotted fowler flap as opposed to a single slotted fowler flap on the A320); additionally some structural strengthening is likely to have been included in key areas.

[9]Although the rated static thrust of the A321neo engines is over 20% greater than that used on the A320, the engines are identical. The added thrust reportedly came from a software update [digital link].

Table 11: Comparison of the mass breakdown of A320-like Aircraft sized in different conceptual design studies. Values are shown in kg with the percentage of the MTOM shown in parentheses. The CSR-01 is from [33] and used the a320-200 as a reference aircraft. The SMR-JA1 is from [14] and used the same reference aircraft as this study.

Parameter	A320	CSR-01	SMR-JA1	B320-JA1	B320-JA1-b
MTOM	79000	77000	79000	79034	76948
OEM	45000 (57.0%)	40965 (53.2%)	44800 (56.7%)	45010 (57.0%)	43481 (56.5%)
Fuselage Mass	-	8986 (11.7%)	10600 (13.4%)	10200 (12.9%)	10004 (13.0%)
Wing Mass	-	8097 (10.5%)	9990 (12.6%)	9001 (11.4%)	8093 (10.5%)
Landing Gear	-	2491 (3.2%)	2670 (3.4%)	2522 (3.2%)	2469 (3.2%)
Propulsion	-	8601 (11.2%)	7660 (9.7%)	7713 (9.8%)	7601 (9.9%)
Empennage	-	1204 (1.6%)	1720 (2.2%)	1720 (2.2%)	1463 (1.9%)
Fuel Systems	-	231 (0.3%)	280 (0.4%)	346 (0.4%)	344 (0.4%)
Furnishings	-	2421 (3.1%)	3600 (4.6%)	2807 (3.6%)	2807 (3.6%)
Operational	-	2188 (2.8%)	-	6962 (8.8%)	6962 (9.0%)
Systems	-	4995 (6.5%)	-	3738 (4.7%)	3738 (4.9%)
Unknown	45000 (57.0%)	1751 (2.3%)	8280 (10.5%)	0 (0.0%)	0 (0.0%)

Other conceptual sizing studies have used the A320 as the reference aircraft, and Table 11 compares a breakdown of the operational mass of the B320-JA1 with two such studies. In general, a good correlation is seen between the three aircraft, and this comparison was used to justify the 15% reduction in landing gear mass applied in Section 2.4.5.

Due to the lack of commercially available data, validating the sizing of liquid-hydrogen-powered aircraft is challenging. Instead, the difference between two aircraft sized with the same TLARs but powered with either kerosene or hydrogen will be compared to that from a similar study [14], which also used the A320neo as the reference aircraft.

Firstly, the TLARs of the A320neo (Table 1) were used to size a kerosene-powered aircraft named the B320-JA1-b. It should be noted that this does not use the 'family' based sizing approach described previously and instead uses the wing loading and load cases of the A320 to size the aircraft. As a result, the B320-JA1-b is 2-tonnes lighter than the B320-JA1-a, with the majority of this weight saving coming from a 10% reduction in wing mass (Table 11).

A hydrogen-powered aircraft was then sized using the same TLARs and will be referred to as the B320-LH2-a. It is assumed that all of the fuel is stored in the aft of the fuselage. As the primary aim of this comparison is to validate structural masses, the maximum capacity of the fuel tank is fixed to that of the other study (5.73 tonnes [14]) and the fuel tank has been sized with the same safety factor (1.25). However, the standard safety factor of 1.5 will be used as the default for the rest of this paper.

Table 12 shows that in both studies, moving to a hydrogen aircraft reduces the MTOM but increases the OEM and specific energy consumption per passenger per km (SEC). The mass breakdown in Table 12 shows that this increase in OEM is primarily driven by the fuel tank and fuselage, with the relative increase in all these parameters comparable across the two studies. The increase in length when moving to hydrogen is also comparable; however, the main differences lie in the estimation of the empennage mass and wing mass.

Regarding empennage mass, the 41% increase in mass in [14] is primarily driven by an increase in the horizontal tail plane area; this is likely driven by the choice of empennage sizing methodologies; this paper uses tail volume coefficients, whereas [14] uses an 'X-plot method'.

Table 12: Comparison between the baseline jet fuel and hydrogen-powered aircraft present in [14] and this paper.

Parameter	SMR-JA1-a	SMR-LH2-b	Δ [%]	B320-JA1	B320-LH2-a	Δ [%]
MTOM [t]	79.1	74.8	-5	77.2	73.4	-5
OEM [t]	44.8	49.8	+11	45.0	43.8	-3
M_{fus} [t]	10.6	13.2	+25	10.0	12.4	+24
M_{wing} [t]	10.0	10.0	0	8.1	8.7	+8
$M_{ht} + M_{vt}$ [t]	1.7	2.4	+41	1.5	1.3	-12
$M_{tank,aft}$ [t]	0	1540	-	0.0	1752.0	-
Fuel Sys. Mass [kg]	280	749	+168	344	766	+123
$M_{f,trip}$ [t]	15	5.73	-62	14.3	5.5	-61
l_{fus} [m]	36.1	45.9	+27	36.9	46.7	+26
S_{wing} [m^2]	122	127	+4.1%	117.9	124.7	+5.8%
$S_h t$ [m^2]	31.7	8.9	+54.2%	28.8	26.4	-8.2%
SEC [kJ/PAX/km]	778	821	+6	653	698	+7

Table 13: A comparison between the baseline kerosene-powered aircraft and hydrogen-powered aircraft design around the harmonic mission (B320-LH2) or a secondary design point (B320-LH2-DP).

Parameter	B320-JA1	B320-LH2	Δ [%]	B320-JA1	B320-LH2-DP	Δ [%]
MTOM [t]	77.3	73.7	-5	77.3	75.3	-3
OEM [t]	42.8	48.6	+14	42.8	49.9	+17
MLND [t]	64.9	68.9	+6	64.9	70.4	+8
Fuel Sys. Mass [t]	0.3	2.7	+689	0.3	3.1	+801
Fuselage Mass [t]	10.0	12.3	+23	10.0	12.8	+28
Wing Mass [t]	8.1	8.7	+8	8.1	9.0	+11
Trip Fuel [t]	12.5	4.8	-61	12.5	4.9	-60
Wing Area [m^2]	117.9	125.2	+6	117.9	127.8	+8
Aspect Ratio	10.9	10.2	-6	10.9	10.0	-8
Length [m]	36.9	46.5	+26	36.9	48.4	+31
CD0 [cnts]	216.4	222.4	+3	216.4	223.0	+3
SEC [kJ/PAX/km]	661.0	707.2	+7	661.0	726.6	+10

This higher fidelity X-plot method likely captures stability criteria that are missed when using tail volume coefficients. However, the mechanism driving this difference is unclear, and this limitation was deemed an acceptable uncertainty of the sizing algorithm.

4 RESULTS

Using the methodology described in Section 2, a baseline JA1 and LH_2 powered aircraft were sized according to the TLARs of the A320WV055 (Table 1). These aircraft are named the B320-JA1 and B320-LH2, respectively, and a comparison of key parameters can be seen in Table 13. The hydrogen-powered aircraft has a lower maximum take-off mass (MTOM), primarily due to the significant reduction in the required fuel mass (LH_2 has an energy density nearly three times that of kerosene). However, the operational empty mass (OEM) of the B320-LH2 is 14% higher due to the mass of the fuel tank and increased fuselage length. The increased OEM increases the landing mass, meaning more wing area is required to achieve the required wing loading, which, coupled with the 'dry' wing configuration, increases the wing mass by 8%. The increased fuselage length and wing area contribute to a larger zero-lift drag coefficient, and overall, the hydrogen-powered aircraft has a specific energy consumption 8% greater than that of the B320-JA1.

The B320-JA1 and the B320-LH2 were sized around the harmonic mission (maximum payload
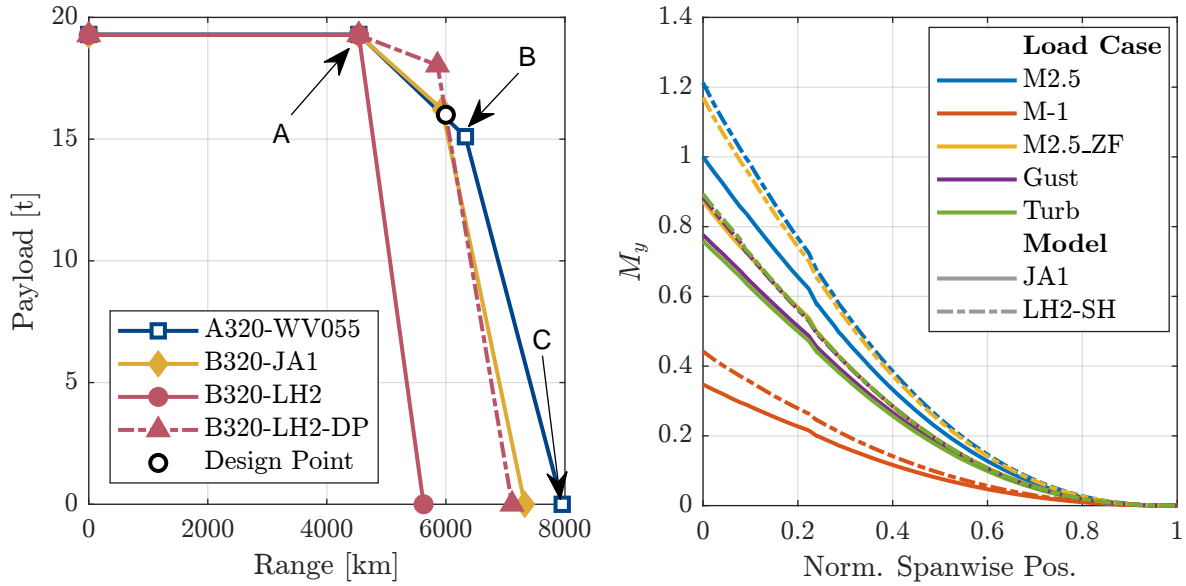
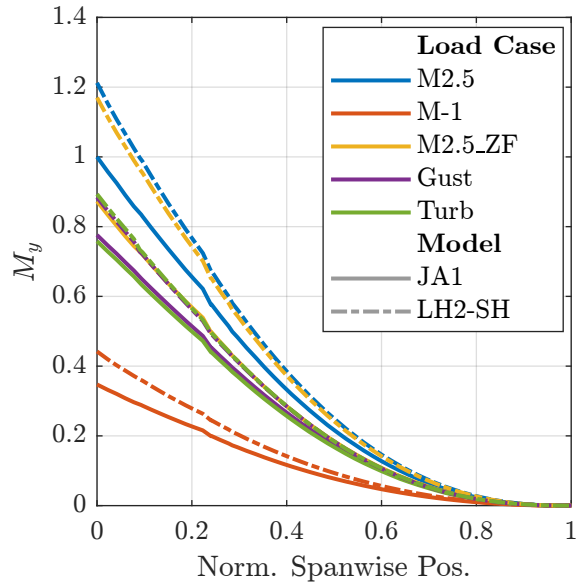Figure 8: Payload range diagram for the A320 and baseline aircraft.

Figure 9: Normalised Wing-root bending moment for the baseline aircraft across multiple load cases.

and take-off mass). However, Fig. 8 shows that the B320-JA1 has a 30% greater ultimate range (range at zero payload and maximum fuel mass) than that of the B320-LH2; the maximum fuel capacity of kerosene-powered aircraft is, in many cases, not a design variable, as it is defined by the volume of the wings which can typically hold more fuel than required for the harmonic mission. Therefore, if the aircraft's payload is reduced, additional fuel can be added (up to the MTOM), increasing the aircraft's range at lower payload fractions. In the case of hydrogen-powered aircraft, this is no longer true. The tank volume of the B320-LH2 was sized to meet the harmonic mission; hence, when the payload is reduced, there is no additional fuel capacity to increase the aircraft's range.

This reduction in maximum range means that comparing the B320-LH2 directly to the B320-JA1 is, in many ways, unfair, as the capabilities of both aircraft vary substantially. The secondary design point is shown in Fig. 8 is added to the sizing algorithm to mitigate this, which ensures that sized aircraft have the same range as the A320 (6000 km) when carrying 83% of the maximum payload. The choice of the secondary design point was arbitrary and could have equally been the ultimate range of the reference aircraft; however, it was chosen on the assumption that the range of a two-class cabin configuration (with fewer passengers and hence less payload) is a more critical design consideration than the ultimate range of an aircraft.

Achieving the secondary design point was integrated into the sizing algorithm by adjusting the minimum additional fuel capacity required during the harmonic mission until both the harmonic mission and secondary design point were achieved. The B320-LH2-DP was sized in this way and is shown in Table 13 to have a 1.5-tonne increase in the MTOM and OEM when compared to the B320-LH2, leading to a further 3% increase in the SEC when compared to the B320-JA1.

The B320-LH2-DP will be used as the baseline hydrogen configuration in the rest of this paper. The nearly one-tonne increase in wing mass when compared to the B320-JA1 is attributed to both an increase in wing area and an increase in wing loads, with Fig. 9 showing the maximum bending moments achieved during a selection of load cases were 20% greater than on the B320-JA1 (The out-of-plane bending moment primarily sizes the wing spars which account for
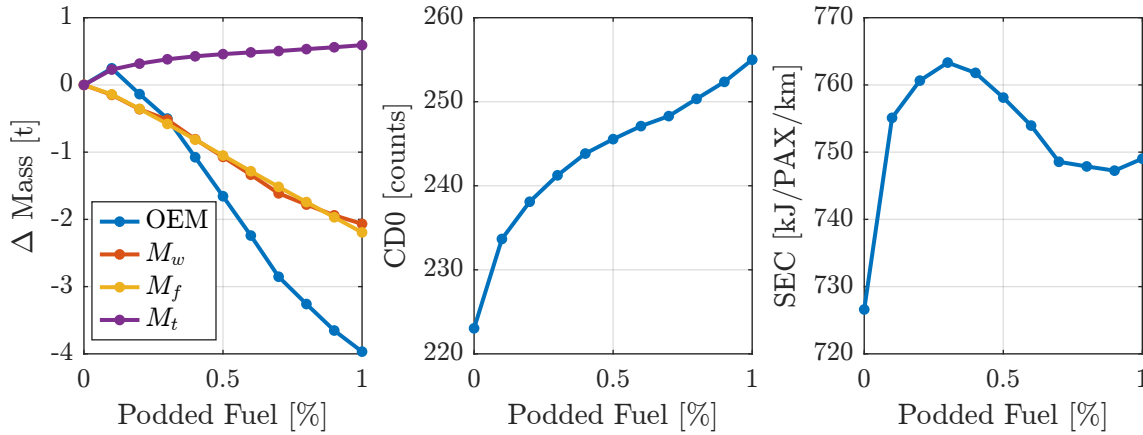
Figure 10: A comparison in the change in mass, zero-lift drag coefficient and specific energy consumption as a function of pod fuel fraction assuming $\eta_y = 0.8$.

over 50% of the sized wing mass). This load increase is primarily attributed to the reduction in inertial relief due to the 'dry' wing configuration and an increase in fuselage mass, which requires a larger force to balance.

A small sensitivity study was conducted with the B320-LH2-DP to highlight the effect of increased mass on the aircraft's SEC. Firstly, the aircraft was sized with an additional one-tonne ballast mounted at the wing's centre, which showed that an additional $3\,\mathrm{m}^2$ of wing area and $630\,\mathrm{kg}$ of structural mass (including $193\,\mathrm{kg}$ of wing mass) is required to support the ballast. Additionally, $136\,\mathrm{kg}$ of extra fuel is required to complete the harmonic mission, increasing the SEC by 2.4%.

Alternatively, if the one-tonne ballast is split into two $500\,\mathrm{kg}$ wingtip masses, the structural mass, wing mass and SEC are $200\,\mathrm{kg}$, $150\,\mathrm{kg}$ and 0.5% lower, respectively, compared to the one-tonne ballast case. Although these differences are marginal, they underline the benefits of increasing the wing's inertial relief.

External fuel tanks would also increase the total drag produced by the aircraft. To highlight this effect, another aircraft was sized without any additional ballast but instead with a 3% increase in the total zero-lift drag coefficient. This increase in drag required $143\,\mathrm{kg}$ of additional fuel to complete the harmonic mission (increasing SEC by 2.6%), requiring an additional $225\,\mathrm{kg}$ of structural mass and $0.4\,\mathrm{m}^2$ of wing area to support. These pseudo-sensitivity studies suggest that the benefits of a 1-tonne weight reduction can be offset by a 3% increase in drag, highlighting the primary trade-off that needs to be considered when assessing the benefits of wing-mounted fuel tanks.

With a drop-tank mounted at 80% of the wingspan, Fig. 10 shows that as the percentage of total fuel stored drop-tank (named the wing fuel fraction (WFF)) is increased to 100%, there is up to a 4-tonne decrease in an aircrafts OEM, with the majority of this decrease coming from a 2-tonne reduction in the fuselage mass and a 2-tonne reduction in the wing mass. However, increasing the WFF also increases the zero-lift drag coefficient by up to 13%, meaning that the SEC of all configurations, including a drop-tank, is worse than that of the aft-only tank configuration.

In the case of a 100% WFF, the 2-tonne reduction in wing mass is driven by a 40% reduction in peak wing loads (Fig. 11). It is important to note that the use of external fuel tanks

(a) Out-of-plane bending (b) Out-of-plane shear force (c) Torsional moment
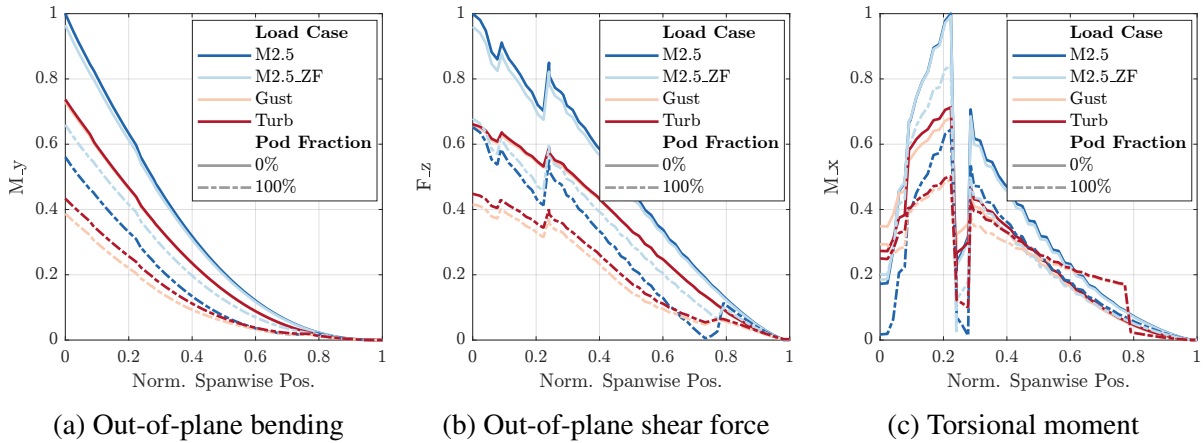
Figure 11: The variation in the three principle spanwise forces and moments applied to the wing in different load cases.
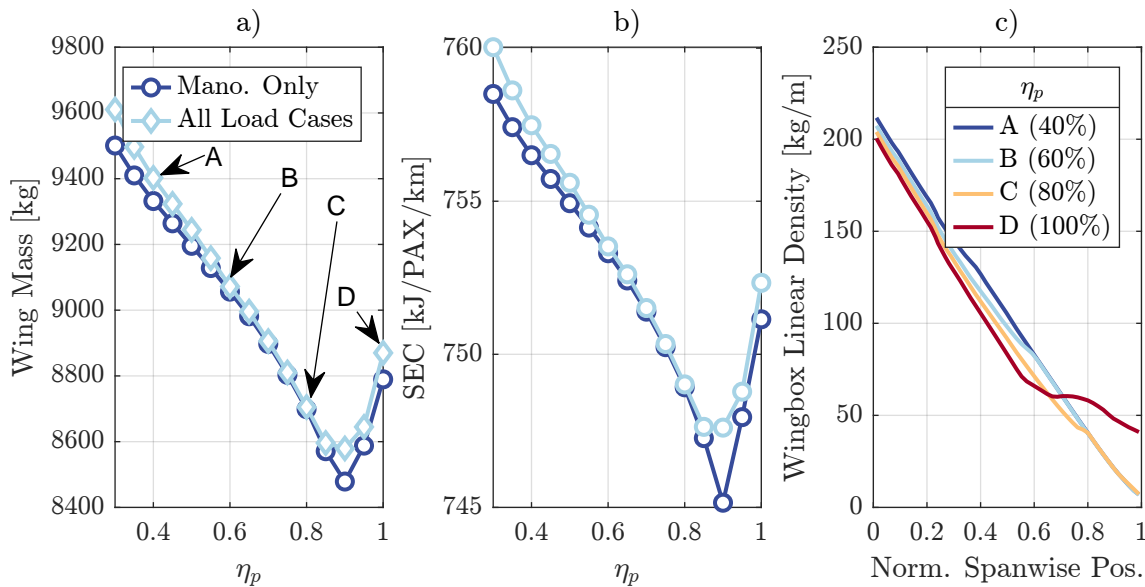

Figure 12: Variation in a) the wing mass and b) the SEC, when the spanwise location of a 100% external fuel tank is varied, and the aircraft is sized with or without gust and turbulence loads. The spanwise linear density of the wingbox at points A, B, C and D in a) is also shown in c).

changes the critical load case at the wing root from the manoeuvre at maximum mass[10] to the zero-fuel manoeuvre, owing to the reduced inertial relief in the zero-fuel case. Most of a wing's mass is located towards the root, and manoeuvre loads dominate the sizing of this wing section. However, gust and turbulence loads become of greater importance in outboard locations, particularly when considering torsional loads, which have the largest impact on skin thickness. It is important to note that gust and turbulence loads typically have similar values in an aft-tank configuration. In contrast, including external fuel tanks increases the relative magnitude of turbulence loads and may adversely affect configurations limited by turbulence.

The limited importance of gust and turbulence loads at the aircraft level is highlighted in the Fig. 12, where dynamic loads increase the wing mass and SEC by a maximum of 1.2% and 0.3%, respectively. Therefore, although simulating dynamic loads are essential to ensure an aircraft is safe to fly, their impact on comparing conceptual designs, at least with smaller

---

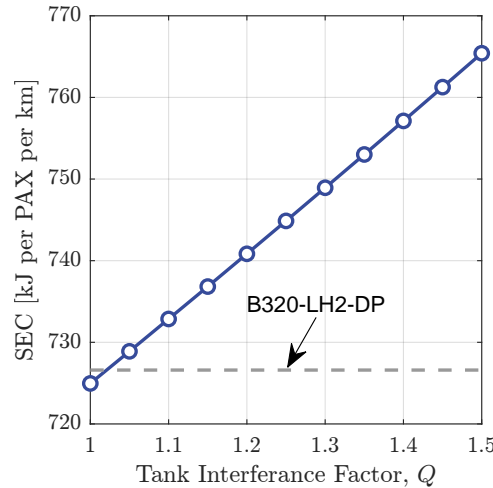[10]taken as the mass at the start of cruise

Figure 13: The effect of varying the interface drag factor of the external fuel tanks between 1 and 1.5. The reference aircraft has a 100% pod-fraction and spanwise position of 80%.

wingspans, is minimal - especially considering the increased computational time required to analyse these load cases.

Fig. 12 also highlights the effect of tank spanwise position on the sized aircraft. The increase in drag from an external tank increases the SEC. If a drop tank is placed close to the wing root, it will provide inertial relief in terms of shear loads but not bending moments, limiting its effectiveness. As the tank is moved outboard, the increase in drag remains constant,[11] however, the inertial relief increases, reducing wing mass and, therefore, reducing the SEC of the aircraft. However, there is a limit to this benefit, and moving the tank beyond 90% of the span increases both wing mass and SEC (Fig. 12). This mass increase when the tank is close to the wingtip can be understood by comparing the spanwise variation in the linear density of the wingbox structure. Fig. 12 shows that moving the tank outboard decreases the wingbox mass inboard of the tank. Below a spanwise tank position of 80%, the wingbox density outboard of the tank remains consistent across configurations. However, in the case of a tank located at the wingtip, there is a significant increase in mass in the outboard sections of the wing, which is likely a function of the wing planform close to the tip, as the relatively small dimensions of the wingbox will necessitate large material thicknesses to support the loads generated by the four-tonne fuel tank. The optimal wing planform is likely different in this configuration, meaning the trends shown in Fig. 12 beyond 90% are likely an artefact of the sizing methodology used in this paper. For this reason, a spanwise position greater than 80% will not be considered for the rest of this paper.

The sizing algorithm makes other assumptions, which may significantly impact the results. One particular assumption is the additional drag produced by drop tanks. Recalling Eq. (21), assumptions were made about the percentage of laminar follow and the interference drag generated by the fuel tank and wing interaction. As suggested by Raymer [12], an interference factor of 1.3 was used when estimating the drag of the drop tank. However, it is also noted in [12] that a value of 1.2 is more suitable for wingtip tanks, and a value of between 1 and 1.5 is plausible, depending on the distance between the tank and the wing. By varying Q between 1 and 1.5, Fig. 13 shows that the SEC of a 100% podded-tank varies between -0.2% and 5.3% of the

---

[11]The drop-tanks drag being independent of spanwise position is a modelling assumption but is not necessarily true.
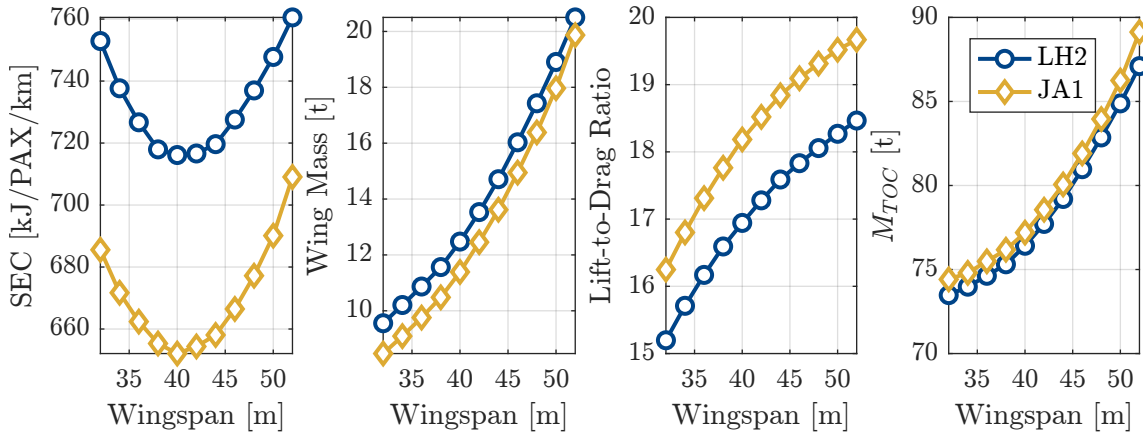
Figure 14: Variation in the a) SEC b) wing mass, c) lift-to-drag ratio, and d) Mass at 'top of climb', as the wingspan of either a jet-fuel or hydrogen-powered aircraft is increased. In the case of hydrogen, an aft-only tank configuration is considered.
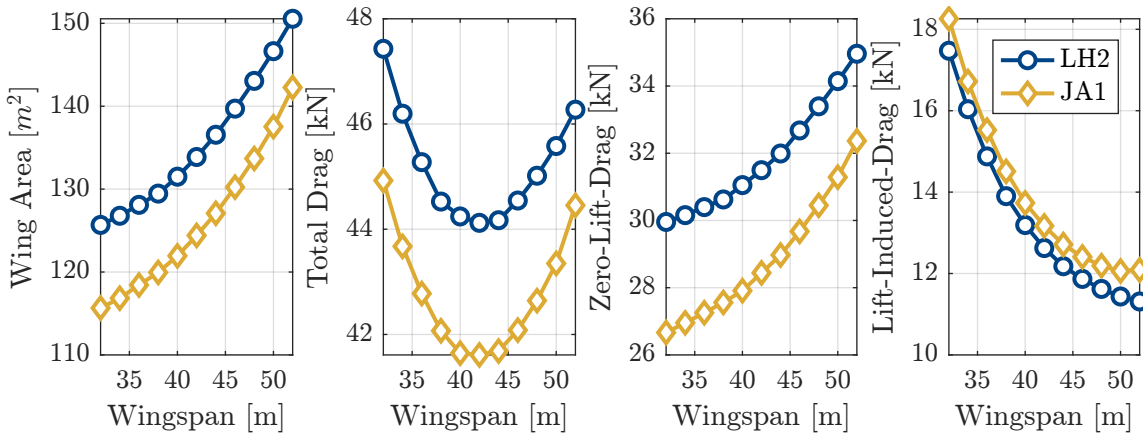

Figure 15: Variation in the a) wing area, b) total drag, c) zero-lift-drag, and d) lift-induced drag, as the wingspan of either a jet-fuel or hydrogen-powered aircraft is increased. All drag estimates are at the 'TOC' condition, and an aft-only tank configuration is considered in the case of hydrogen.

baseline B320-LH2-DP. This variation in the interference factor can be thought of as improved integration of the fuel tank with the wing or through an increase in laminar flow along the pod. They highlight that a well-integrated tank design (with 22% less drag than currently estimated) could result in an aircraft with a similar SEC to an aft-only tank configuration.

Conceptually, the idea that 100% podded fuel tanks could have a similar SEC opens up other interesting questions, particularly when considering the certification of hydrogen aircraft. Due to the small molecular size of hydrogen gas, it is liable to leak from the fuel system [1]; hence, storing and transporting hydrogen within the fuselage may add a significant fire risk for passengers. Therefore, podded fuel tanks, in which the fuel is solely stored away from the fuselage,[12] may provide a configuration which is easier to homologate. This is not to say that the drop tanks do not have their own challenges; ground clearance during take-off and landing will be a critical concern, as will the increased moments of inertia of the aircraft; fuel tanks placed far from the centre of mass will increase roll inertia and may adversely couple with dynamics associated with yawing, such as the aircraft's Dutch-roll mode and recovery from a flat-spin.

So far, this study has only considered aircraft with a wingspan of $36\,\mathrm{m}$. However, at larger

---

[12]Although there may still be a requirement for cross-flow systems between the wings

wingspans, the maximum bending moments experienced by a wing increase (as loads are moved outboards, increasing their moment arm), meaning the benefits of inertial relief may become more significant. Figs. 14 and 15 compare the effect of increasing the wingspan of the baseline kerosene and hydrogen-powered aircraft (with a WFF of 0%). As the wingspan is increased, both aircraft follow a broadly similar trend; wing mass increases with wingspan, and this increased mass compounds at the aircraft level, where approximately $300\,\mathrm{kg}$ of additional mass and $2.2\,\mathrm{m}^2$ of wing area are required to support each additional tonne of wing mass. This increase in mass is countered by an increased lift-to-drag ratio (L/D), and at low wingspans, the benefits of an increased L/D outweigh the drag penalty due to the increased mass, leading to a reduction in the SEC (Fig. 14).

However, at larger wingspans, the rate of change in the wing mass increases, and the lift-to-drag ratio decreases. This means an optimal wingspan exists where the increased mass cancels out the benefits of an increased lift-to-drag ratio and where, beyond this value, the SEC begins to increase with the wingspan. For both baseline aircraft, this optimal wingspan lies at around $40\,\mathrm{m}$, corresponding to an aspect ratio of approximately 12. It is important to note that this optimal aspect ratio is significantly lower than the 20 quoted in the previous study using the same wingbox sizing methodology [2]. In the previous paper, only the wingbox was sized, and the wing area and other masses were held constant, whereas, at an aircraft level, the increased wing mass requires more wing area to support (creating more skin-friction drag) and requires other changes, such as larger, more powerful, engines and stronger landing gear. These compounding effects significantly decrease the optimal aspect ratio.

However, the methodology used to estimate the secondary wing mass in this paper may be too conservative. As described in section Section 2.7, the secondary mass is estimated as 73.7% of the primary mass [16]. This empirical relationship uses statistical trends from existing aircraft but may not be well suited to varying the aspect ratio of the same aircraft. Other methodologies relate the secondary mass to a wing's planform area [7]; this would have resulted in a roughly 75% slower increase in secondary mass, pushing the optimal wingspan out to a larger value. However, it is unclear which methodology best matches reality, and this dependency will be explored further in future work.

Moving back to hydrogen-powered aircraft, Figs. 16 and 17 compare the effect of increasing the wingspan on LH_2 powered configurations with either an aft-fuel tank (a WFF of 0%) or external wing-mounted fuel tanks (a WFF of 100%). It is shown that although the inertial relief provided by drop-tanks pushes the optimal wingspan from $40\,\mathrm{m}$ to $42\,\mathrm{m}$ metres, the optimal SEC is still 2.2% greater than the aft-only configuration. It is important to remember that when modelling a span over $35\,\mathrm{m}$, a hinge is added at a span of $35\,\mathrm{m}$ and the drop is located $1.5\,\mathrm{m}$ inboard of this hinge; therefore, as the span is increased the normalised spanwise position of the drop-tank decreases, limiting the inertial relief provided by the tank. This limitation was chosen because it would seem infeasible to lift the tank with the hinge mechanism and transfer cryogenic liquid across it.

Currently, the sizing process has assumed a constant technology level (e.g. aluminium construction) with zero load alleviation. Using lighter materials such as carbon composites or load alleviation devices will reduce the weight penalty of increasing the wingspan - pushing the optimal wingspan to a higher value. To simulate this, the two hydrogen configurations were sized with a reduced safety factor of one, corresponding to a 33% reduction in peak loads. In the aft configuration, Fig. 16 shows this reduction in loads reduces the wing mass by 19% at the lowest
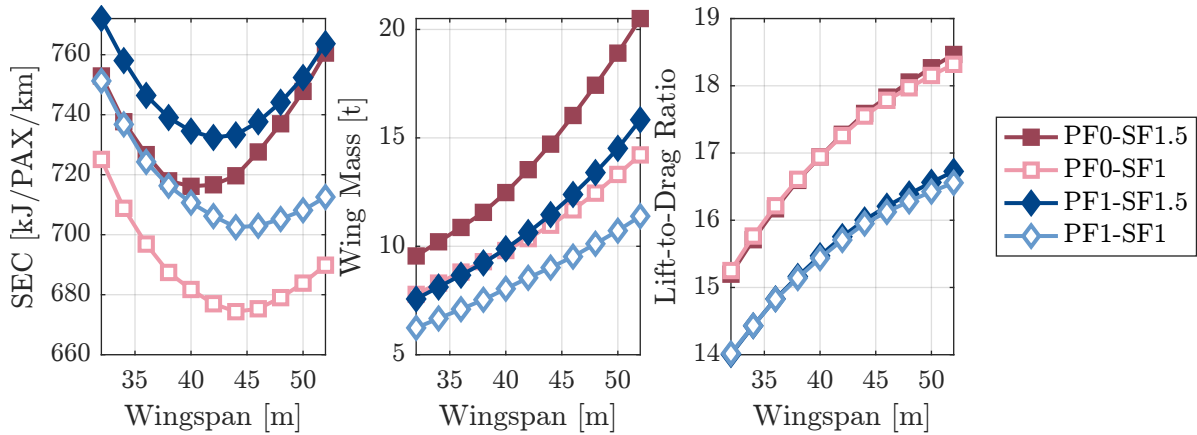
Figure 16: Variation in the a) SEC, b) wing mass, and c) lift-to-drag ratio, as the wingspan of an aircraft is increased with either an aft-only or pod-only fuel configuration and a safety factor of 1.5 or 1. PF'X'-SF'Y' means a pod fraction of 'X' and a safety factor of 'Y'.
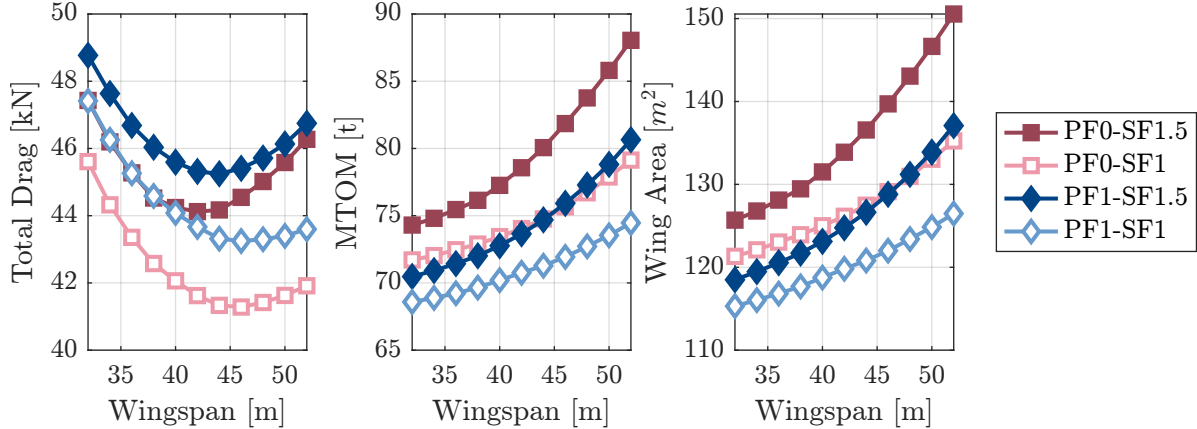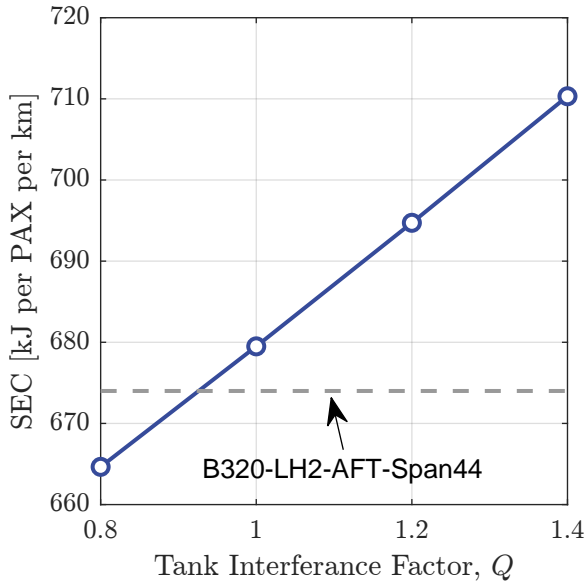

Figure 17: Variation in the a) Total drag, b) MTOM, and c) wing area, as the wingspan of an aircraft is increased with either an aft-only or pod-only fuel configuration and a safety factor of 1.5 or 1. PF'X'-SF'Y' means a pod fraction of 'X' and a safety factor of 'Y'.

Figure 18: The effect of varying the interference drag factor of 100% drop tanks between 1 and 1.5, with a wingspan of $44\,\mathrm{m}$.
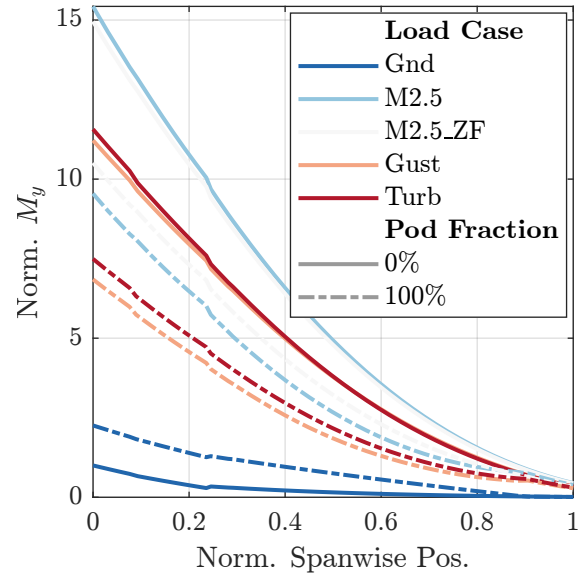
Figure 19: The variation in the maximum out-of-plane bending moment applied to the wing in different load cases, for a span of $44\,\mathrm{m}$.

wingspan and 30% at the highest, which pushes the optimal wingspan out to $44\,\mathrm{m}$ (which is an aspect ratio of approximately 14) and reduces the SEC by 5.9%. The drop-tank configuration has a similar optimal wingspan, but the minimum SEC is now 4.2% greater than the aft case (compared to 2.2% at a safety factor of 1.5). Furthermore, at a wingspan of $44\,\mathrm{m}$, Fig. 18, shows that the drag generated by the drop-tank would need to decrease by 37% (1.3 is the default value of Q) for the aircraft to match the SEC of the aft-only configuration.

As a final point, Fig. 19 shows the critical load cases of the optimal aft-only and drop-tank configurations with a safety factor of 1. It shows that the critical load case has not changed with increasing wingspan, with the zero-fuel manoeuvre still dominating the critical loads. A similar trend is seen in the other forces and moments, with dynamic loads becoming of greater importance towards the tip - particularly for torsional moments.

5 CONCLUSIONS

This study explored the aerodynamic and structural implications of integrating liquid hydrogen (LH_2) fuel tanks in medium-sized commercial aircraft with high aspect ratio wings. The analysis used a multidisciplinary conceptual aircraft sizing methodology, considering both fuselage-stored and wing-mounted hydrogen fuel tank configurations. The wingbox structure was sized using numerical simulations of manoeuvres, gust and turbulence encounters using an equivalent aeroelastic model. It was shown that integrating wing-mounted hydrogen fuel tanks can provide significant inertial relief, reducing wing mass by over 20%. However, despite this reduction in wing mass, the increased parasitic drag from external fuel tanks generally outweighs the reduction in lift-induced drag, resulting in less favourable fuel efficiency metrics for aircraft with wing-mounted tanks. This conclusion was observed across a range of wingspans with a reduction in fuel efficiency of 2.2% at lower spans and up to 4.2% reduction at larger spans. Although this is a conceptual study with many assumptions, the drag generated by the external tank would need to be reduced by approximately 40% to match the fuel efficiency of the fuselage-only tank configuration, suggesting that permanently attached wing-mounted fuel tanks are not a viable configuration for hydrogen-powered aircraft with high aspect ratio wings.

REFERENCES

[1] Adler, E. J. and Martins, J. R. R. A. (2023). Hydrogen-powered aircraft: Fundamental concepts, key technologies, and environmental impacts. *Progress in Aerospace Sciences*, 141, 100922. ISSN 0376-0421, `https://doi.org/10.1016/j.paerosci.2023.100922`.

[2] Gu, H., Healy, F., Rezgui, D., et al. (2022). Sizing of high-aspect-ratio wings with folding wingtips. *Journal of Aircraft*, 1–15. ISSN 0021-8669, `https://doi.org/10.2514/1.C036908`.

[3] Calderon, D., Cooper, J., Lowenberg, M., et al. (2019). Sizing high-aspect-ratio wings with a geometrically nonlinear beam model. *Journal of Aircraft*, 56(4), 1455–1470. ISSN 0021-8669, `https://doi.org/10.2514/1.C035296`.

[4] Silberhorn, D., Atanasov, G., Walther, J.-N., et al. (2019). Assessment of hydrogen fuel tank integration at aircraft level.

[5] Brewer, G. D. (1991). *Hydrogen Aircraft Technology*. Boca Raton, FL: CRC Press. ISBN 9780849358388.

[6] Tinling, B. E. and Kolk, W. R. (1951). The effects of centrally mounted wing-tip tanks on the subsonic aerodynamic characteristics of a wing of aspect ratio 10 with 35 degrees of sweepback. Tech. rep.

[7] Torenbeek, E. (2013). *Advanced Aircraft Design*. Aerospace Series. Nashville, TN: John Wiley and Sons. ISBN 9781118568118, `https://doi.org/10.1002/9781118568101`.

[8] Anon. (2020). Certification specifications and acceptable means of compliance for large aeroplanes cs-25 amendment 26. Tech. rep., Easa.

[9] Anon. (2023). Easy access rules for air operations — revision 21. Tech. rep., Agency, European Union Aviation Safety.

[10] Lambe, A. B. and Martins, J. R. R. A. (2012). Extensions to the design structure matrix for the description of multidisciplinary design, analysis, and optimization processes. *Structural and Multidisciplinary Optimization*, 46(2), 273–284. ISSN 1615-1488, `https://doi.org/10.1007/s00158-012-0763-y`.

[11] Gudmundsson, S. (2021). *General Aviation Aircraft Design: Applied Methods and Procedures*. Oxford, England: Butterworth-Heinemann. ISBN 9780128226476.

[12] Raymer, D. P. (2018). *Aircraft Design: A Conceptual Approach*. Aiaa Education Series. Reston, VA: American Institute of Aeronautics and Astronautics, 6 ed. ISBN 9781624104909, `https://doi.org/10.2514/4.104909`.

[13] Proesmans, P.-J. and Vos, R. (2022). Airplane design optimization for minimal global warming impact. *Journal of Aircraft*, 59(5), 1363–1381. ISSN 0021-8669, `https://doi.org/10.2514/1.C036529`.

[14] Onorato, G., Proesmans, P., and Hoogreef, M. F. M. (2022). Assessment of hydrogen transport aircraft. *CEAS Aeronautical Journal*, 13(4), 813–845. ISSN 1869-5590, `https://doi.org/10.1007/s13272-022-00601-6`.

[15] Lukaczyk, T. W., Wendorff, A. D., Colonno, M., et al. (2015). *Suave: An Open-Source Environment for Multi-Fidelity Conceptual Vehicle Design*. Aiaa Aviation Forum. American Institute of Aeronautics and Astronautics, `https://doi.org/10.2514/6.2015-3087`.

[16] Chambers, M. C., Ardema, M. D., Patron, A. P., et al. (1996). Analytical fuselage and wing weight estimation of transport aircraft. Tech. Rep. NASA-TM-110392, NASA.

[17] Wöhler, S., Atanasov, G., Silberhorn, D., et al. (2020). Preliminary aircraft design within a multidisciplinary and multifidelity design environment.

[18] Cavagna, L., Ricci, S., and Travaglini, L. (2011). Neocass: An integrated tool for structural sizing, aeroelastic analysis and mdo at conceptual design level. *Progress in Aerospace Sciences*, 47(8), 621–635. ISSN 0376-0421, `https://doi.org/10.1016/j.paerosci.2011.08.006`.

[19] Anon. (2020). A320 - aircraft characteristics airport and maintenance planning. Tech. rep., Airbus S.A.S., Blagnac, France.

[20] Verstraete, D., Hendrick, P., Pilidis, P., et al. (2010). Hydrogen fuel tanks for subsonic transport aircraft. *International Journal of Hydrogen Energy*, 35(20), 11085–11098. ISSN 0360-3199, `https://doi.org/10.1016/j.ijhydene.2010.06.060`.

[21] Anon. (2020). A319 - aircraft characteristics airport and maintenance planning. Tech. rep., Airbus S.A.S., Blagnac, France.

[22] Anon. (2020). A321 - aircraft characteristics airport and maintenance planning. Tech. rep., Airbus S.A.S., Blagnac, France.

[23] Torenbeek, E. (1982). *Synthesis of Subsonic Airplane Design*. Dordrecht, Netherlands: Kluwer Academic, 1982 ed. ISBN 9789024727247.

[24] Kretov, A. and Tiniakov, D. (2022). Evaluation of the mass and aerodynamic efficiency of a high aspect ratio wing for prospective passenger aircraft. *Aerospace*, 9(9), 497. ISSN 2226-4310, `https://doi.org/10.3390/aerospace9090497`.

[25] Anon. (2023). Type-certification data sheet for engine leap-1a and leap-1c series engines. Tech. Rep. EASA.E.110, European Union Aviation Safety Agency.

[26] Niṭă, M. and Scholz, D. (2012). Estimating the oswald factor from basic aircraft geometrical parameters. In *Deutscher Luft- und Raumfahrtkongress*.

[27] Anon. (2018). *Quick Reference Guide*. Msc Nastran 2018. MSC Software GmbH.

[28] Wright, J. and Cooper, J. E. (2015). *Introduction to Aircraft Aeroelasticity and Loads*. Aerospace Series. Chichester UK: Wiley. ISBN 978-1-118-48801-0, `https://doi.org/10.1002/9781118700440`.

[29] Albano, E. and Rodden, W. P. (1969). A doublet-lattice method for calculating lift distributions on oscillating surfaces in subsonic flows. *AIAA Journal*, 7(2), 279–285. ISSN 0001-1452, `https://doi.org/10.2514/3.5086`.

[30] Kalman, T. P., Rodden, W. P., and Giesing, J. P. (1971). Application of the doublet-lattice method to nonplanar configurations in subsonic flow. *Journal of Aircraft*, 8(6), 406–413, `https://doi.org/10.2514/3.59117`.

[31] Giesing, J. P., Kalman, T. P., and Rodden, W. P. (1972). Subsonic steady and oscillatory aerodynamics for multiple interfering wings and bodies. *Journal of Aircraft*, 9(10), 693–702, `https://doi.org/10.2514/3.59066`.

[32] Van Heerden, A. S. J., Guenov, M. D., and Molina-Cristóbal, A. (2019). Evolvability and design reuse in civil jet transport aircraft. *Progress in Aerospace Sciences*, 108, 121–155. ISSN 0376-0421, `https://doi.org/10.1016/j.paerosci.2019.01.006`.

[33] Abu Salem, K., Palaia, G., Quarta, A. A., et al. (2023). Medium-range aircraft conceptual design from a local air quality and climate change viewpoint. *Energies*, 16(10). ISSN 1996-1073, `https://doi.org/10.3390/en16104013`.

COPYRIGHT STATEMENT